Baseline Optimization for Spatial-Temporal Coupling in Geosynchronous Differential Synthetic Aperture Radar Tomography

Xichao Dong, *Member, IEEE*, Yan Liu, Zhiyang Chen, Xinyan Chen, Yuanhao Li, *Member, IEEE*, Cheng Hu, *Senior Member, IEEE*, and Feifeng Liu, *Member, IEEE*

***Abstract*—Differential synthetic aperture radar tomography (D-TomoSAR) uses multiple SAR acquisitions at different times to form an elevation-time 2-D synthetic aperture, enabling recovery of the target's 3-D structure and deformation velocity. However, the imaging performance of D-TomoSAR is influenced by the spatial-temporal baseline distribution, which is one of the crucial factors. Due to the difference in orbit altitude, the effects of various perturbation forces on geosynchronous SAR (GEO SAR) are significantly different from those on low Earth orbit SAR (LEO SAR), leading to different geometries in the spatial-temporal baseline distributions of GEO SAR and LEO SAR in the repeat-pass acquisitions. The spatial-temporal baseline distribution of LEO SAR is random, while that of GEO SAR is coupled. Although GEO SAR obtains a large number of acquisitions due to the short repeat-pass time, using data under all spatial-temporal baselines for D-TomoSAR does not necessarily provide the best imaging results. Therefore, how to select spatial-temporal baselines that can improve the estimation accuracy is important. In this article, the Cramér–Rao lower bound of GEO D-TomoSAR estimation accuracy is determined by considering multiple factors, including baseline decorrelation and spatial-temporal coupling. The optimal spatial-temporal baseline selection is modeled as a multiobjective problem and solved by the Nondominated Sorting Genetic Algorithm II (NSGA-II). Given the absence of in-orbit GEO SAR and the orbital similarity between GEO SAR and BeiDou Inclined Geosynchronous Orbit (IGSO) satellite, the real ephemeris of BeiDou IGSO satellite is used to simulate the baseline distribution of GEO SAR and verify the baseline optimization method.**

***Index Terms*—Baseline optimization, coupling, differential synthetic aperture radar tomography (D-TOMOSAR), geosynchronous synthetic aperture radar (GEO SAR), spatial-temporal baseline.**

Manuscript received 16 May 2023; accepted 24 September 2023. Date of publication 18 October 2023; date of current version 23 November 2023. This work was supported in part by the National Natural Science Foundation of China under Grant 61960206009, Grant 61971039, and Grant 62201051, in part by China Postdoctoral Science Foundation under Grant 2022M720443, in part by the Natural Science Foundation of Shandong Province under Grant ZR2022QF067, and in part by the National Key Research and Development Program of China under Grant SQ2022YFB3900055. *(Corresponding author: Zhiyang Chen.)*

Xichao Dong is with the Radar Research Laboratory, School of Information and Electronics, Beijing Institute of Technology, Beijing 100081, China, and also with the Beijing Institute of Technology Chongqing Innovation Center, Chongqing 401120, China (e-mail: xcdong@foxmail.com).

Yan Liu, Xinyan Chen, Yuanhao Li, Cheng Hu, and Feifeng Liu are with the Radar Research Laboratory, School of Information and Electronics, Beijing Institute of Technology, Beijing 100081, China, and also with the Key Laboratory of Electronic and Information Technology in Satellite Navigation, Ministry of Education, Beijing Institute of Technology, Beijing 100081, China (e-mail: liuyan_nrd@163.com; chenxinyan1998@163.com; lyh.900101@163.com; cchchb@163.com; feifengliu_bit@bit.edu.cn).

Zhiyang Chen is with the Radar Research Laboratory, School of Information and Electronics, Beijing Institute of Technology, Beijing 100081, China, also with the Key Laboratory of Electronic and Information Technology in Satellite Navigation, Ministry of Education, Beijing Institute of Technology, Beijing 100081, China, and also with the Advanced Technology Research Institute, Beijing Institute of Technology, Jinan 250300, China (e-mail: zychen12@163.com).

Digital Object Identifier 10.1109/JSTARS.2023.3325584

I. Introduction

DIFFERENTIAL synthetic aperture radar (SAR) tomography (D-TomoSAR) is a multibaseline, multitemporal SAR interferometry technique that combines the unique characteristics of differential SAR interferometry (D-InSAR) and SAR tomography (TomoSAR). D-TomoSAR uses a stack of SAR images acquired from multiple passes of an SAR system at different times to reconstruct the reflectivity of scatterers along elevation and deformation velocity. This enables 3-D reconstruction and deformation monitoring of the scene, also known as 4-D SAR imaging [1], [2].

The high-resolution images provided by new-generation SAR sensors such as TerraSAR-X and COSMO-Skymed have been used in D-TomoSAR for urban infrastructure reconstruction, enabling the detection of deformation at the millimeter level [3], [4], [5]. Low Earth orbit (LEO) SAR systems currently in operation have an orbital altitude of less than 1000 km, which limits their coverage area and results in long revisit periods. The repeat-pass time for common LEO SAR systems is up to several days; in some cases, it can be several weeks. As a result, it usually takes around a year or more to form a stack of SAR images that can be used for D-TomoSAR imaging. However, extended temporal baselines can introduce temporal decorrelation effects, which decrease scene coherence and negatively affect the performance of differential tomography.

Geosynchronous SAR (GEO SAR) [6], [7] operates at an altitude of approximately 36 000 km and offers a significantly shorter repeat-pass time compared to LEO SAR. Furthermore, the beam width can reach thousands of kilometers, enabling effective large-scale and near-continuous observations [8]. Scholars in this field have conducted comprehensive and in-depth research on both near-zero inclination GEO SAR and inclined GEO SAR. So far, there has been relatively mature research on key technologies such as GEO SAR system design [9], [10], orbit design [11], and imaging algorithms [12], [13], [14].

Furthermore, extensive research has demonstrated and applied GEO SAR to InSAR for height measurement and D-InSAR for deformation inversion [15]. This has also given rise to many new configurations of GEO SAR, including GEO spaceborne-airborne bistatic SAR imaging [16], [17] and formation-flying GEO SAR [18], [19]. With appropriate orbit parameter design, GEO SAR can also be used for 3-D imaging of scenes, such as circular SAR (CSAR) [20] and tomographic SAR (TomoSAR) [21]. Multibaseline GEO SAR imaging was first proposed by Hu et al. [21] in 2019 and was experimentally validated using the BeiDou IGSO satellite.

The advantage of GEO SAR with strong timeliness in observations is beneficial for D-TomoSAR. However, the extension of imaging from LEO to GEO requires consideration of the differences in their baseline distribution.

1) The elevation resolution is closely related to the spatial baseline span. In LEO SAR, the spatial baseline span is relatively small, typically in the range of hundreds of meters, so the elevation resolution is poor. For example, the elevation resolution of the TerraSAR-X system is roughly 50 times worse than that of the azimuth or range direction [22]. The spatial baseline span of GEO SAR can reach hundreds of kilometers, forming a large synthetic aperture in the elevation direction and improving the elevation Rayleigh resolution. However, at the same time, excessively long spatial baselines can lead to baseline decorrelation, which reduces the correlation between images.
2) Different spatial-temporal baseline patterns can affect the results of D-TomoSAR imaging, which was identified in [23] and [24]. In LEO SAR, the distribution relationship between spatial and temporal baselines is random. However, in GEO SAR, due to perturbation effects, the position of the satellite drifts over time, and the correlation between the spatial and temporal baselines is obvious, showing a high degree of coupling. The coupled spatial-temporal baselines deteriorate the performance of the formed 2-D synthetic aperture, affecting the estimation accuracy of elevation and deformation velocity.

Current research in D-TomoSAR has mainly focused on improving imaging algorithms and introducing complex deformation models to obtain optimal estimates of elevation and deformation information using methods such as spectral estimation or compressive sensing [2], [25], [26]. However, limited attention has been paid to optimizing the performance of D-TomoSAR by directly constructing it from the SAR data stack. When it comes to the research of imaging performance of D-TomoSAR, Sun [27] derived from the D-TomoSAR signal model that the accuracy of elevation and deformation estimation is related to spatial-temporal baseline in the presence of noise. Reale et al. [28] considered the influence of thermal dilation on small deformations of scenes, and under usual spatial baseline distributions, the estimation performance depends on the geometry of temperature and time distribution. These studies are primarily based on LEO SAR systems and cannot address the unique challenges presented by GEO SAR.

This article presents a detailed analysis of the GEO SAR spatial-temporal baseline characteristics, highlighting the differences in the geometrical distribution of the spatial-temporal baseline between GEO SAR and LEO SAR. Under the short-term acquisition, the coupling is easily formed between the GEO SAR temporal and spatial baselines. The estimation accuracy of elevation and deformation mean velocity is analyzed by deriving the Cramér–Rao lower bound (CRLB) under the framework of GEO D-TomoSAR, which emphasizes the limitations of acquisition characteristics on the estimation accuracy. Finally, a method for optimizing the spatial-temporal baseline in GEO D-TomoSAR is proposed by selecting suitable satellite positions to achieve a more favorable spatial-temporal baseline distribution.

The structure of this article is as follows. Section II briefly reviews the imaging principles of D-TomoSAR, introduces the spatial-temporal baseline distribution characteristics of GEO SAR. Section III theoretically analyzes the CRLB of GEO D-TomoSAR under the influence of decorrelation, to describe the limit of estimation accuracy. Section IV establishes a spatial-temporal baseline optimization model for GEO D-TomoSAR and solves it based on the Nondominated Sorting Genetic Algorithm II. Section V presents simulation experiments to verify the effectiveness of the proposed method and discusses in depth the simulation results of GEO D-TomoSAR imaging before and after baseline optimization under different cases. Finally, Section VI concludes this article.

II. GEO D-TomoSAR Model and Baseline Analysis

A. D-TomoSAR Imaging Model

Assuming the SAR sensor with wavelength λ makes N acquisitions of the same scene with small deformation at different times and spatial locations, a stack of SAR images is constructed. After registration, deramping, and phase error compensation, the focused complex value g_n of a range-elevation pixel collected for the nth acquisition at time t_n is [1]

$$g_n = \int_{\Delta s} \gamma(s) e^{j2\pi[\xi_n s + 2d(s,t_n)/\lambda]} ds \tag{1}$$

where $\gamma(s)$ represents the reflectivity function along elevation s, and $\xi_n = 2b_n/(\lambda r)$ denotes the spatial frequency with respect to the spatial baseline b_n, and r is the distance between the antenna phase center at the master image acquisition time and the reference point on the scene. $d(s,t_n)$ represents the deformation of the scatterer in elevation s and temporal baseline t_n, which is typically related to subsidence and geophysical phenomena [29]. The geometry of D-TomoSAR imaging is illustrated in Fig. 1.

In the case of linear deformation, performing Fourier expansion on $e^{j4\pi d(s,t_n)/\lambda}$ yields $e^{j4\pi d(s,t_n)/\lambda} = \int_{\Delta v} p(s,v) e^{j2\pi\eta_n v} dv$, where $p(s,v)$ is a peak function related to height and deformation velocity. Therefore, (1) can be written as

$$g_n = \int_{\Delta s}\int_{\Delta v} \gamma(s,v) e^{j2\pi(\xi_n s + \eta_n v)} ds dv \tag{2}$$

where $\gamma(s,v) = \gamma(s)p(s,v)$, and $\eta_n = -2t_n/\lambda$ represents the temporal frequency with respect to the temporal baseline t_n.

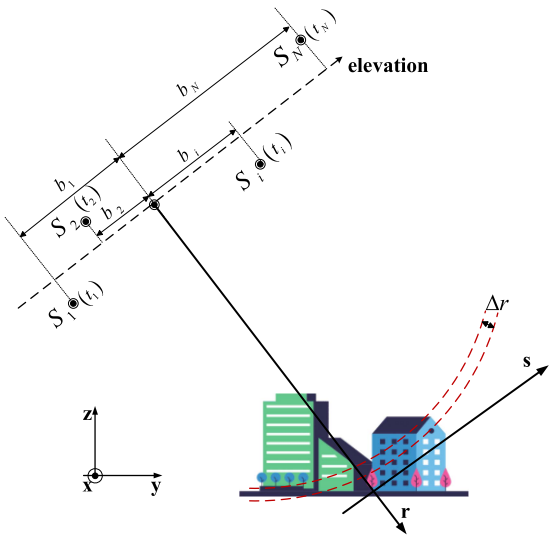

Fig. 1. D-TomoSAR geometry. The single-channel SAR sensor makes a total of N acquisitions of the scene at different times.

By uniformly discretizing the elevation s and mean deformation velocity v with step sizes Δs and Δv, respectively, the discrete signal model of (2) can be written as

$$g_n = \sum_{i=1}^{N_s}\sum_{j=1}^{N_v}\gamma(s_i, v_j)\exp(j2\pi\xi_n s_i)\exp(j2\pi\eta_n v_j),$$
$$n = 1, 2, \ldots, N \tag{3}$$

where N_s and N_v denote the number of sampled points in the elevation and mean deformation velocity directions, respectively, and the total number of samples is $M = N_s N_v$. In the presence of noise ε, the D-TomoSAR imaging model can be rewritten in matrix form as

$$\mathbf{g} = \mathbf{R}\boldsymbol{\gamma} + \boldsymbol{\varepsilon} \tag{4}$$

where $\mathbf{g} = [g_1, g_2, \ldots, g_N]^T$ is the $N \times 1$ vector of complex measurements obtained from the stack of SAR images, and $\boldsymbol{\gamma} = [\gamma(s_1, v_1), \gamma(s_1, v_2), \ldots, \gamma(s_1, v_{Nv}), \gamma(s_2, v_1), \ldots, \gamma(s_{N_s}, v_{Nv})]^T$ is the $M \times 1$ vector of unkown reflectivity on elevation-velocity (EV) plane. $\mathbf{R} = [R_1, R_2, \ldots, R_N]^T$ is the $N \times M$ mapping matrix, and the mth row element can be expressed as $R_n = \frac{1}{\sqrt{M}}[p_n \otimes q_n]$, where the symbol $\otimes$ denotes Kronecker product, and p_n and q_n are noted as

$$p_n = [\exp(j2\pi\xi_n s_1), \exp(j2\pi\xi_n s_2), \ldots, \exp(j2\pi\xi_n s_{N_s})]^T$$
$$q_n = [\exp(j2\pi\eta_n v_1), \exp(j2\pi\eta_n v_2), \ldots \exp(j2\pi\eta_n v_{N_v})]^T. \tag{5}$$

B. GEO SAR Baseline Distribution

GEO SAR operates in the geosynchronous orbit at an altitude of approximately 36 000 km. Depending on the orbit inclination, it can be classified into inclined GEO SAR and near-zero inclination GEO SAR. The inclined GEO SAR carried out in the high inclination with a "large figure-8" ground track and the medium inclination with a "small figure-8" ground track. Satellites operating in high orbits are subject to perturbations beyond the earth's gravity, including atmospheric drag, lunar, and solar gravitational forces, and solar radiation pressure. Due to these perturbations, the orbital parameters of a GEO SAR satellite change over time, causing the actual orbital trajectory to deviate from the predetermined position [30]. To accurately determine the position of a GEO SAR satellite and analyze its baseline characteristics, we use the high-precision orbit perturbation (HPOP) model in the System Tool Kit (STK) software to simulate the orbital motion of the satellite under the influence of perturbations. The HPOP model in STK can accurately simulate complex perturbations such as atmospheric drag, third-body gravitational forces, and solar radiation pressure, and generate high-precision satellite orbits.

Whether from the SAR datasets formed by LEO SAR or GEO SAR, the elevation resolution ρ_s and deformation resolution ρ_v of D-TomoSAR are related to the total span of the spatial and temporal baselines

$$\rho_s = \frac{\lambda r}{2B}$$
$$\rho_v = \frac{\lambda}{2T} \tag{6}$$

where B is the total span of the spatial baseline (perpendicular baseline) and T is the total span of the temporal baseline. To avoid spectrum aliasing, according to the Nyquist sampling theorem, the unambiguous range of D-TomoSAR imaging in elevation and deformation directions is determined by the average spatial baseline interval Δb and the average temporal baseline interval Δt, which can be expressed as

$$H_{\text{Unambiguous}} \leq \frac{\lambda r}{2\Delta b}$$
$$V_{\text{Unambiguous}} \leq \frac{\lambda}{2\Delta t}. \tag{7}$$

For the reconstruction of elevation and deformation information in D-TomoSAR, it is necessary to ensure the good coherence of scatterers in the entire scene. When the types of objects in the scene are determined, and the errors of quantization and registration are small, the coherence between acquired data is mainly related to the coherence of the baseline, time, and signal-to-noise ratio (SNR) [31]. In general, the longer the spatial baseline, the more sensitive the SAR system is to elevation changes, but the coherence between the signals obtained from the two acquisitions decreases as the baseline length increases. As for the temporal baseline, the longer it is, the better the resolution in the deformation direction, but the temporal decorrelation becomes stronger. The GEO SAR's short repeat-pass time can effectively reduce the impact of temporal decorrelation. However, the spatial decorrelation caused by its baseline length of hundreds of kilometers cannot be ignored.

Spatial baseline decorrelation leads to the reduction of baseline correlation. Baseline correlation ρ_{Bas} is mainly affected by perpendicular baseline b_n, and its expression is

$$\rho_{\text{Bas}} = 1 - \frac{b_n}{B_{\text{crit}}} \tag{8}$$

TABLE I
GEO SAR AND LEO SAR ORBIT PARAMETERS FOR STK DEMONSTRATION

Orbital Parameters	GEO SAR	LEO SAR
Semi-major axis (*km*)	42163.9	7003.52
Eccentricity	0	0.00118
Orbital inclination (°)	16	97.86
Angle of periapsis (°)	0	90
longitude of the ascending node (°)	90	50

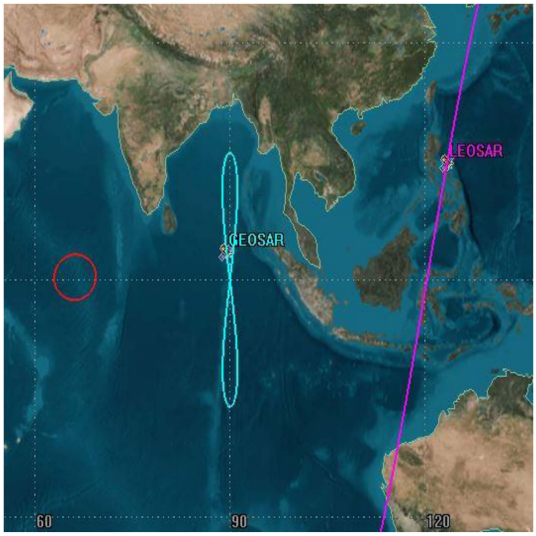

Fig. 2. Ground tracks of GEO SAR and LEO SAR in STK.

where B_{crit} is the critical baseline, which is mainly related to the incident angle θ of radar at the target. Let c be the speed of light, BW be the bandwidth, and the formula for B_{crit} is

$$B_{\text{crit}} = \frac{\lambda r \tan\theta}{c}\text{BW}. \tag{9}$$

In this article, we choose the "small figure-8" GEO SAR orbit scheme, whose orbit parameters are shown in Table I. According to the given parameters, the GEO SAR's and LEO SAR's ground tracks obtained in STK are shown in Fig. 2, where the ground track of GEO SAR forms a figure-8 shape and the ground track of LEO SAR approximates a straight line. The red circle represents the beam coverage of the GEO SAR at the position shown in the figure. Without any orbit control, we simulate the operation of GEO SAR for 120 days to obtain the GEO SAR position under multiple acquisitions, and the imaging scene is located in the center of the beam on the ground. Taking the first acquisition as a reference, the calculated perpendicular baseline is shown by the blue dot in Fig. 3, while the red line is the critical baseline length based on the incidence angle of the scene.

Despite the lack of an in-orbit operational GEO SAR system at the moment, we can use the spatial-temporal baseline distribution of the BeiDou Inclined Geosynchronous Orbit (IGSO) satellite to demonstrate the characteristics of the GEO SAR spatial-temporal baseline because of the similarity between their

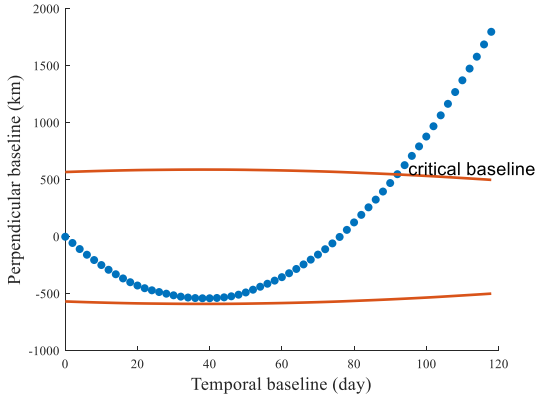

Fig. 3. Spatial-temporal baseline distribution (blue dot) and critical baseline (red line) of GEO SAR without orbit control.

orbits. Fig. 4(a) shows the spatial-temporal baseline distribution of 90 passes of the BeiDou IGSO satellite with 180 days (Data from [32]), and Fig. 4(b) presents the spatial-temporal baseline distribution of 28 passes of COSMO- SkyMed (CSK) acquired within one year. The baseline distribution of the two indicates that BeiDou IGSO can obtain a large number of acquisitions in a short time, which greatly improves the correlation of data. Moreover, the spatial baseline span of BeiDou IGSO is much longer than CSK, thus making the elevation resolution higher than CSK. However, unlike the random and disordered distribution of CSK, the spatial-temporal baseline of BeiDou show regular changes and the overall curve distribution. In the case of fewer acquisitions and shorter time, the spatial-temporal baseline of BeiDou is even almost completely correlated, namely, spatial-temporal baseline coupling, as shown in the red box of Fig. 4(a).

III. ESTIMATION ACCURACY

D-TomoSAR can be regarded as a 2-D parameter estimation problem in the EV plane. The CRLB reflects the optimal accuracy achievable in parameter estimation using the available information. Only noise interference on the estimation is taken into account in the D-TomoSAR imaging model. For GEO SAR, the issue of spatial decorrelation under a long spatial baseline cannot be neglected. As a result, the approach of directly deriving the likelihood function from the imaging model to get the parameter estimate CRLB [33] is unsuitable for estimating D-TomoSAR accuracy under the effect of several decorrelations. In this section, the GEO D-TomoSAR 4-D reconstruction accuracy is discussed from the perspective of SAR images stack.

Given that N is the total number of single-look complex (SLC) images used in D-TomoSAR, $\hat{\mathbf{Z}}_k = [Z_1^k, Z_2^k, \ldots, Z_N^k]^T$ is the complex value corresponding to the kth pixel of the SAR images stack (see Fig. 5), and the probability density function corresponding to $\hat{\mathbf{Z}}_k$ is [28]

$$f(\hat{\mathbf{Z}}_k) = \frac{1}{\pi^N |\mathbf{C}_k|} \exp(-\hat{\mathbf{Z}}_k^H \mathbf{C}_k^{-1} \hat{\mathbf{Z}}_k). \tag{11}$$

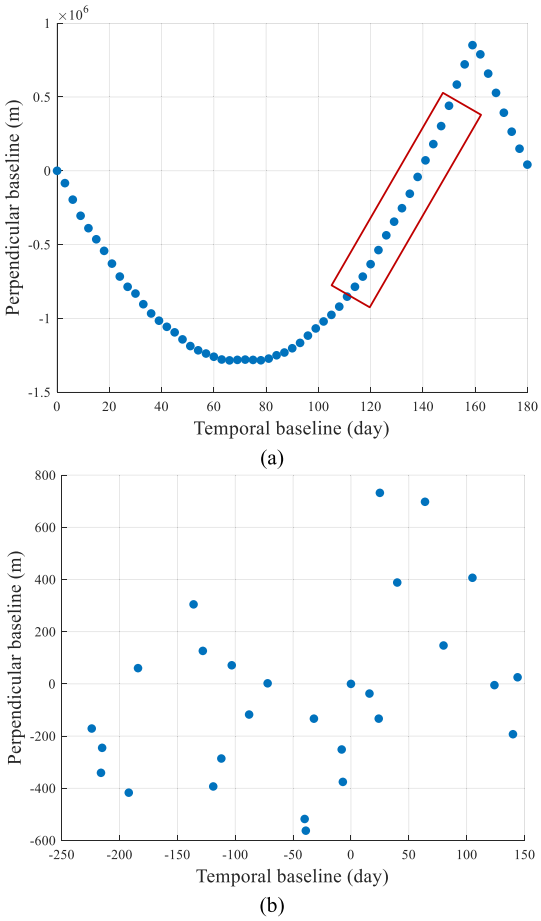

Fig. 4. Comparison of GEO SAR and LEO SAR spatial-temporal baseline distribution. (a) 90-pass baseline of BeiDou IGSO has a more regular distribution of spatial-temporal baseline, especially in the red box, where the spatial-temporal baseline is almost linear. (b) 28-pass baseline of CSK with random spatial-temporal baseline distribution.

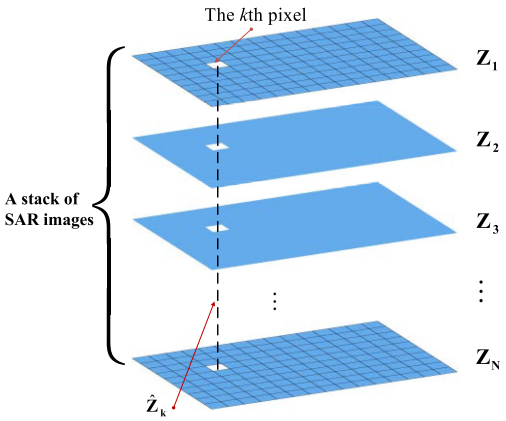

Fig. 5. k th pixel in the stack of SAR images forms $\hat{\mathbf{Z}}_k$.

The likelihood function for the parameter vector $\boldsymbol{\theta} = [s, v]^T$ derived from the probability density function (11) for a single scatterer is

$$f(\boldsymbol{\theta}) = \ln[f(\hat{\mathbf{Z}}_k|\boldsymbol{\theta})]$$

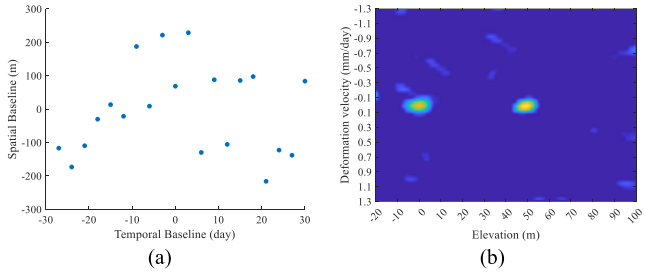

Fig. 6. Imaging under random distribution of spatial-temporal baseline. (a) Spatial-temporal baseline of random distribution. (b) Reflectivity of the two scatters is reconstructed in the EV plane. The elevation and deformation information of the two scatterers can be clearly distinguished.

$$= -\ln(\pi^N |\mathbf{C}|) - \hat{\mathbf{Z}}_k^H \mathbf{C}_k^{-1} \hat{\mathbf{Z}}_k. \tag{12}$$

The covariance matrix $\mathbf{C}$ can be decomposed into the product of the amplitude matrix and the phase matrix to simplify as [34]

$$\mathbf{C} = \boldsymbol{\Phi}^* \boldsymbol{\Gamma} \boldsymbol{\Phi} \tag{13}$$

where the forms of $\boldsymbol{\Phi}$ and $\boldsymbol{\Gamma}$ are shown in (10) shown at the bottom of next page and (14), respectively. $\boldsymbol{\Gamma}$ represents the coherence matrix in which the element ρ are the product of multiple correlation factors. When considering baseline correlation, signal-to-noise ratio correlation, and temporal correlation, $\rho_{i,j} = \rho_{\text{Bas}} \cdot \rho_{\text{SNR}} \cdot \rho_{\text{Tem}}$. Furthermore, there are $|\boldsymbol{\Phi}^* \boldsymbol{\Gamma} \boldsymbol{\Phi}| = |\boldsymbol{\Phi}^*| \cdot |\boldsymbol{\Gamma}| \cdot |\boldsymbol{\Phi}| = |\boldsymbol{\Phi}^*| \cdot |\boldsymbol{\Phi}| \cdot |\boldsymbol{\Gamma}| = |\boldsymbol{\Gamma}|$ and $(\boldsymbol{\Phi}^* \boldsymbol{\Gamma} \boldsymbol{\Phi})^{-1} = \boldsymbol{\Phi}^{-1} \boldsymbol{\Gamma}^{-1} (\boldsymbol{\Phi}^*)^{-1} = \boldsymbol{\Phi}^* \boldsymbol{\Gamma}^{-1} \boldsymbol{\Phi}$, where

$$\boldsymbol{\Gamma} = \begin{bmatrix} 1 & \rho_{1,2} & \cdots & \rho_{1,N} \\ \rho_{1,2} & 1 & \cdots & \rho_{2,N} \\ \vdots & \vdots & \ddots & \vdots \\ \rho_{1,N} & \rho_{2,N} & \cdots & 1 \end{bmatrix}. \tag{14}$$

Computing the inverse of the Fisher information matrix (FIM) will obtain the CRLB for the parameter vector $\boldsymbol{\theta}$ as

$$\text{var}(\hat{\theta}_i) \geq [\mathbf{I}^{-1}(\boldsymbol{\theta})]_{ii} \tag{15}$$

where $[\mathbf{I}(\boldsymbol{\theta})]_{ij} = -E[\frac{\partial^2 f(\boldsymbol{\theta})}{\partial \theta_i \partial \theta_j}]$, $i = 1, 2; j = 1, 2$. Based on the properties of matrix partial derivatives and trace, the resulting FIM of size 2×2 is

$$\mathbf{I}(\boldsymbol{\theta}) = 2 \begin{bmatrix} tr(\boldsymbol{\Lambda}_\mathbf{s} \boldsymbol{\Gamma}^{-1} \boldsymbol{\Lambda}_\mathbf{s} \boldsymbol{\Gamma} - \boldsymbol{\Lambda}_\mathbf{s}^2) & tr(\boldsymbol{\Lambda}_\mathbf{s} \boldsymbol{\Gamma}^{-1} \boldsymbol{\Lambda}_\mathbf{v} \boldsymbol{\Gamma} - \boldsymbol{\Lambda}_\mathbf{s} \boldsymbol{\Lambda}_\mathbf{v}) \\ tr(\boldsymbol{\Lambda}_\mathbf{s} \boldsymbol{\Gamma}^{-1} \boldsymbol{\Lambda}_\mathbf{v} \boldsymbol{\Gamma} - \boldsymbol{\Lambda}_\mathbf{s} \boldsymbol{\Lambda}_\mathbf{v}) & tr(\boldsymbol{\Lambda}_\mathbf{v} \boldsymbol{\Gamma}^{-1} \boldsymbol{\Lambda}_\mathbf{v} \boldsymbol{\Gamma} - \boldsymbol{\Lambda}_\mathbf{v}^2) \end{bmatrix} \tag{16}$$

where Λ_s and Λ_v are the diagonal matrices formed by the spatial frequency and temporal frequency, respectively, denoted as follows:

$$\Lambda_s = 2\pi \begin{bmatrix} \xi_1 & 0 & \cdots & 0 \\ 0 & \xi_2 & \cdots & 0 \\ \vdots & \vdots & \ddots & \vdots \\ 0 & 0 & \cdots & \xi_N \end{bmatrix}$$

$$\Lambda_v = 2\pi \begin{bmatrix} \eta_1 & 0 & \cdots & 0 \\ 0 & \eta_2 & \cdots & 0 \\ \vdots & \vdots & \ddots & \vdots \\ 0 & 0 & \cdots & \eta_N \end{bmatrix}. \tag{17}$$

The inverse matrix for the FIM of (16) results in (23), shown at the bottom of this page, where the factor W is expressed as

$$W = [\mathrm{tr}(\mathbf{\Lambda_v \Gamma^{-1} \Lambda_v \Gamma - \Lambda_v^2})][\mathrm{tr}(\mathbf{\Lambda_s \Gamma^{-1} \Lambda_s \Gamma - \Lambda_s^2})] - [\mathrm{tr}(\mathbf{\Lambda_s \Lambda_v - \Lambda_s \Gamma^{-1} \Lambda_v \Gamma})]^2. \tag{18}$$

Therefore, taking into account the impact of decorrelation factors, the standard deviation of the elevation and mean deformation velocity estimates are

$$\sigma_s \geq \sqrt{\frac{tr(\mathbf{\Lambda_v \Gamma^{-1} \Lambda_v \Gamma - \Lambda_v^2})}{2W}} \tag{19}$$

$$\sigma_v \geq \sqrt{\frac{tr(\mathbf{\Lambda_s \Gamma^{-1} \Lambda_s \Gamma - \Lambda_s^2})}{2W}}. \tag{20}$$

The aforementioned is the estimation accuracy of GEO D-TomoSAR for single scatter imaging under the influence of various decorrelations. If only the impact of noise on imaging is considered, we consider that the SNR under different acquisitions is roughly identical, and the correlation coefficient matrix can be viewed as having elements with the same value except for the diagonal, expressed as

$$\mathbf{\Gamma} = \begin{bmatrix} 1 & \rho & \dots & \rho \\ \rho & 1 & \dots & \rho \\ \vdots & \vdots & \ddots & \vdots \\ \rho & \rho & \dots & 1 \end{bmatrix} \tag{21}$$

where $\rho = (1 + \mathrm{SNR}^{-1})^{-1}$ is the SNR correlation. FIM shown in (16) degenerates into

$$\mathbf{I}(\theta)_{\mathrm{SNR}} = \frac{8\pi^2\rho^2N^2}{1+\rho(N-2)-\rho^2(N-1)} \begin{bmatrix} \mathrm{var}(\xi) & \mathrm{cov}(\xi\eta) \\ \mathrm{cov}(\xi\eta) & \mathrm{var}(\eta) \end{bmatrix} \tag{22}$$

where $\gamma_{\xi,\eta} = \frac{\mathrm{cov}(\xi\eta)}{\sqrt{\mathrm{var}(\eta)\mathrm{var}(\xi)}}$ represents the correlation coefficient between space frequency ξ and temporal frequency η, then inverse matrix of $\mathbf{I}(\theta)_{\mathrm{SNR}}$ is (as follows: (24) shown at the bottom of this page,

We can use the Taylor series to approximate $\rho \approx 1 - \mathrm{SNR}^{-1}$ and $\rho^2 \approx 1 - 2\mathrm{SNR}^{-1}$ when the SNR is high. As a result, in this case, the accuracy of elevation and mean deformation velocity estimation in D-TomoSAR can be expressed as

$$\sigma_s = \frac{\lambda r}{4\pi\sqrt{2N \cdot \mathrm{SNR} \cdot \mathrm{var}(b)(1-\gamma_{b,t}^2)}} \tag{25}$$

$$\sigma_v = \frac{\lambda}{4\pi\sqrt{2N \cdot \mathrm{SNR} \cdot \mathrm{var}(t)(1-\gamma_{b,t}^2)}} \tag{26}$$

where $\gamma_{b,t}$ is the correlation coefficient between spatial baseline and temporal baseline.

It should be noted that, in comparison to the CRLB of TomoSAR, the estimation accuracy of D-TomoSAR in elevation and mean deformation velocity depends on the spatial-temporal baseline correlation coefficient in addition to the number of SAR acquisitions and SNR. The more random the distribution of spatial-temporal baselines, the smaller the spatial-temporal correlation coefficient, and the better the estimation performance. Conversely, when the spatial-temporal baseline coupling is higher, it becomes more difficult to distinguish between the two parameters of height and deformation velocity, leading to poorer estimation performance. As seen in Fig. 6, there are scatterers at heights of 0 and 50 m in locations where there is no deformation. D-TomoSAR can reconstruct the distribution of each of the two scatterers in the EV plane when the temporal and spatial baselines are distributed randomly, but it is challenging to separate the elevation and deformation information of the scatterers when the baselines are distributed linearly (see Fig. 7). Therefore, to address the issue of high coupling between the

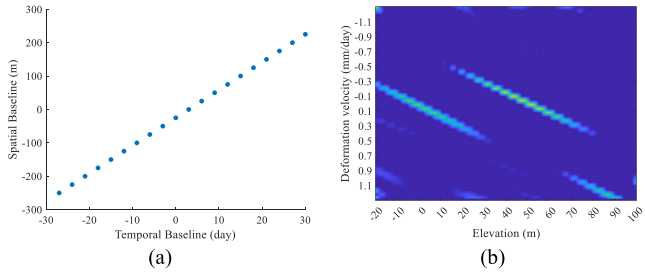

(a) (b)

Fig. 7. Imaging under a linearly distributed spatial-temporal baseline. (a) Linear distribution of the space-time baseline. (b) Reflectivity of the two scatters is reconstructed in the EV plane. The elevation and deformation information cannot be obtained clearly.

$$\mathbf{\Phi} = \begin{bmatrix} \exp[j2\pi(\xi_1 s + \eta_1 v)] & 0 & \dots & 0 \\ 0 & \exp[j2\pi(\xi_2 s + \eta_2 v)] & \dots & 0 \\ \vdots & \vdots & \ddots & \vdots \\ 0 & 0 & \dots & \exp[j2\pi(\xi_N s + \eta_N v)] \end{bmatrix} \tag{10}$$

$$\mathbf{I^{-1}}(\theta) = \frac{1}{2W} \begin{bmatrix} \mathrm{tr}(\mathbf{\Lambda_v \Gamma^{-1} \Lambda_v \Gamma - \Lambda_v^2}) & \mathrm{tr}(\mathbf{\Lambda_s \Lambda_v - \Lambda_s \Gamma^{-1} \Lambda_v \Gamma}) \\ \mathrm{tr}(\mathbf{\Lambda_s \Lambda_v - \Lambda_s \Gamma^{-1} \Lambda_v \Gamma}) & \mathrm{tr}(\mathbf{\Lambda_s \Gamma^{-1} \Lambda_s \Gamma - \Lambda_s^2}) \end{bmatrix} \tag{23}$$

$$\mathbf{I}^{-1}(\theta)_{\mathrm{SNR}} = \frac{1+\rho(N-2)-\rho^2(N-1)}{8\pi^2\rho^2N^2 \cdot \mathrm{var}(\xi) \cdot \mathrm{var}(\eta) \cdot (1-\gamma_{\xi,\eta}^2)} \begin{bmatrix} \mathrm{var}(\eta) & -\mathrm{cov}(\xi\eta) \\ -\mathrm{cov}(\xi\eta) & \mathrm{var}(\xi) \end{bmatrix}. \tag{24}$$

temporal and spatial baselines in GEO SAR, a step needs to be added to the imaging process to deal with the spatial-temporal baseline problem. Otherwise, it will significantly degrade the 4-D reconstruction performance.

IV. Baseline Optimization Based on NSGA-II

For the following two main reasons, the spatial-temporal baseline distribution and selection in LEO D-TomoSAR have not attracted a lot of attention:

1) the LEO SAR repeat-pass time is long, the data needed in differential tomography is time-consuming, and the amount of data collected is little;
2) the spatial-temporal baseline distribution of LEO SAR is random.

However, the short repeat-pass time for GEO SAR enables the acquisition of a lot of data in a relatively short time. Without any treatment, using all obtained data for D-TomoSAR increases the computing complexity of the imaging process and degrades imaging performance due to the existing spatial-temporal baseline coupling. As a result, in GEO -TomoSAR imaging processing, it is necessary to perform baseline optimization. In this section, an optimal spatial-temporal baseline selection model is constructed to choose a set of optimal spatial-temporal baseline distributions from all of the spatial-temporal baseline data of GEO SAR. The model is based on the CRLB of elevation and deformation estimation and takes into account the characteristics of the GEO SAR baseline.

A. Baseline Optimization Model

The spatial-temporal baseline optimization for GEO D-TomoSAR can be considered a multiobjective optimization problem. Based on the Rayleigh theory, larger baseline spans provide a higher Rayleigh resolution, but result in increased decorrelation and phase noise. Conversely, smaller baseline spans reduce decorrelation but lead to poor Rayleigh resolution. By Nyquist's sampling theorem, increasing the average sampling interval reduces the maximum unblurred height, making it impossible to image targets beyond the limit. To account for the effects of baseline parameters in the GEO D-TomoSAR system, several factors must be considered, such as the distribution, span, interval, and numbers of spatial-temporal baselines. The spatial-temporal correlation coefficient $\gamma_{b,t}$, which primarily characterizes the distribution pattern of the spatial-temporal baseline, is a crucial indicator in evaluating the performance of the 2-D synthetic aperture of the EV plane. As such, it should be given priority in selecting the optimal spatial-temporal baseline pattern.

In addition, the average interval between the spatial baselines of GEO SAR is large. To expand the imaging range in the elevation direction as much as possible and avoid ambiguous in imaging results, the maximum unambiguous height needs to be included as an optimization objective. Because of the short repeat-pass time of GEO SAR, the temporal baseline interval is small regardless of baseline selection. In slowly deforming scenarios, the deformation velocity does not readily introduce ambiguity. Furthermore, assuming a constant SNR across temporal baselines, it remains an intrinsic property of the imaging system.

Suppose the GEO SAR system makes N acquisitions of the same scene, numbered $1, 2, \ldots, N$ in order, and the corresponding satellite spatial position is $\mathbf{P} = [p_1, p_2, \ldots, p_N]^T$ and time is $\mathbf{D} = [d_1, d_2, \ldots, d_N]^T$. With $x_i = 1$ indicating that the ith acquisition is selected and $x_i = 0$ indicating that the ith acquisition is not selected, the decision vector $\mathbf{X} = [x_1, x_2, \ldots, x_N]^T$ denotes the selection strategy for these N acquisitions.

Let Ω represent the index of gene values equal to 1 on a chromosome. $\mathbf{P}_\Omega$ and $\mathbf{D}_\Omega$ denote the matrices formed by extracting the elements corresponding to Ω from matrices $\mathbf{P}$ and $\mathbf{D}$, i.e.,

$$\left.\begin{aligned} &\Omega = \{\{l_1, l_2, \ldots, l_n\} : x_{l_n} = 1\} \\ &\mathbf{P}_\Omega = [p_{l_1}, p_{l_2}, \ldots, p_{l_n}] \\ &\mathbf{D}_\Omega = [d_{l_1}, d_{l_2}, \ldots, d_{l_n}] \end{aligned}\right\}. \tag{27}$$

Based on the selected satellite positions and times, a new set of spatial baselines $\mathbf{B}^{\mathbf{X}} = [b_1, b_2, \ldots b_n]^T$ and temporal baselines $\mathbf{T}^{\mathbf{X}} = [t_1, t_2, \ldots, t_n]^T$ are created, where n is equal to the sum of the elements 1 in $\mathbf{X}$. From this, the correlation coefficient and the maximum unambiguous height under this set of spatial-temporal baselines can be calculated.

The optimization objective is set as follows:

$$\begin{aligned} \min \gamma_{b,t} &= \frac{\operatorname{cov}(\mathbf{B}^{\mathbf{X}}\mathbf{T}^{\mathbf{X}})}{\sqrt{\operatorname{var}(\mathbf{B}^{\mathbf{X}})} \cdot \sqrt{\operatorname{var}(\mathbf{T}^{\mathbf{X}})}} \\ \max H_{\max} &= \frac{\lambda r}{2 \cdot \Delta b^{\mathbf{X}}} \end{aligned} \tag{28}$$

where $\Delta b^{\mathbf{X}}$ is the average baseline interval for $\mathbf{B}^{\mathbf{X}}$.

In GEO SAR, the effects of baseline decorrelation and SNR decorrelation are mainly considered. Suppose $b_{i,j}$ denotes the spatial baseline between the ith SAR image and the jth image, and B_c^i represents the critical baseline with the ith image as the master image. $\rho_{\text{Bas}}^{i,j}$ stands for the baseline correlation between the ith SAR image and the jth image, with

$$\rho_{\text{Bas}}^{i,j} = \begin{cases} 1 - \frac{b_{i,j}}{B_c^i}, & b_{i,j} < B_c^i \\ 0, & \text{else} \end{cases}. \tag{29}$$

If the SNR correlation approximation to ρ_{SNR}, the correlation coefficient matrix is

$$\Gamma = \begin{bmatrix} 1 & \rho_{\text{SNR}}\rho_{\text{Bas}}^{1,2} & \cdots & \rho_{\text{SNR}}\rho_{\text{Bas}}^{1,n_x} \\ \rho_{\text{SNR}}\rho_{\text{Bas}}^{2,1} & 1 & \cdots & \rho_{\text{SNR}}\rho_{\text{Bas}}^{2,n_x} \\ \vdots & \vdots & \ddots & \vdots \\ \rho_{\text{SNR}}\rho_{\text{Bas}}^{n_x,1} & \rho_{\text{SNR}}\rho_{\text{Bas}}^{n_x,2} & \cdots & 1 \end{bmatrix}. \tag{30}$$

In the case of reconstruction of sparse signal using the compressed sensing theory, according to the restricted isometry property (RIP), the number of acquisitions need to satisfy $N_t = O(K \log(M/K))$ [33], where M is the number of columns of mapping matrix $\mathbf{R}$, and K is the sparsity, to achieve high accuracy reconstruction of the sparse vector $\boldsymbol{\gamma}$ in differential tomography. So, the total number of selected acquisitions n

should satisfy $n > N_t$. The values of σ_s and σ_v are calculated based on (19) and (20), which satisfy $\sigma_s < T_s$ and $\sigma_v < T_v$, respectively, where T_s and T_v are the predetermined threshold values. N_{unc}^k is used to denote the count of elements in row k of $\mathbf{\Gamma}$ for which $\mathbf{\Gamma}_{k,j} < \beta$, where β is the set correlation coefficient threshold. We consider that below this threshold, the correlation between the selected kth and the jth acquisition is weak. Using $\gamma_{\text{unc}}^k = N_{\text{unc}}^k/n$ to represent the proportion of weak correlations in row k of $\mathbf{\Gamma}$, a smaller ratio indicates a higher number of effective observations. This must satisfy $\gamma_{\text{unc}}^k < T_c$, where T_c is the threshold.

In summary, the GEO D-TomoSAR optimal baseline selection mathematical model is expressed as (31).

B. Model Solution

Multiobjective optimization is the simultaneous optimization of multiple subobjectives, and there are often certain "interest" conflicts between these subobjectives, so the final set of compromise solutions is obtained, called the Pareto optimal solution set or nondominated solution set, and then, through certain decision rules to find the most satisfactory solution. As a common multiobjective optimization algorithm, NSGA-II has the advantages of high computational efficiency, strong robustness, and easy understanding [35]. In this section, the baseline optimization practical problem is combined with NSGA-II, and the following strategies are used to solve the model:

$$\begin{aligned} &\min \gamma_{b,t} \\ &\max H_{\max} \\ &\text{s.t.} \begin{cases} \mathbf{X} = [x_1, x_2, x_3 \ldots, x_N] \\ x_i = 0 \text{ or } 1, (i = 1, 2, \ldots, N) \\ n = \sum_{i=1}^{N} x_i > N_t \\ \gamma_{\text{unc}}^k = N_{\text{unc}}^k/n < T_c, (k = 1, 2, \ldots, n) \\ \sigma_s = \sqrt{\frac{tr(\mathbf{\Lambda_v \Gamma^{-1} \Lambda_v \Gamma - \Lambda_v^2})}{2W}} < T_s \\ \sigma_v = \sqrt{\frac{tr(\mathbf{\Lambda_s \Gamma^{-1} \Lambda_s \Gamma - \Lambda_s^2})}{2W}} < T_v \end{cases} . \end{aligned} \tag{31}$$

1) Population Initialization: Under the binary encoding strategy, a chromosome of length N is randomly generated and denoted as $\mathbf{X} = [x_1, x_2, \ldots, x_N]$, where each x_i represents a gene with two possible values, 0 or 1. A value of $x_i = 1$ indicates the selection of the ith observation, while $x_i = 0$ represents the exclusion of the ith observation. In addition, each chromosome represents an individual, leading to the creation of N_p individuals to form the initial population. Each individual represents a potential baseline selection scheme, as shown in Fig. 8.

2) Genetic Manipulation: The crossover operation adopts a uniform crossover strategy, while the mutation is based on the simple mutation strategy. The offspring population formed after crossover and mutation is merged with the parent population to form a new population with a size of $2N_p$. In order to ensure the diversity of chromosomes in the merged new population, duplicate individuals within the population are first removed, and then, randomly generated chromosomes are added to maintain the size of the population as $2N_p$.

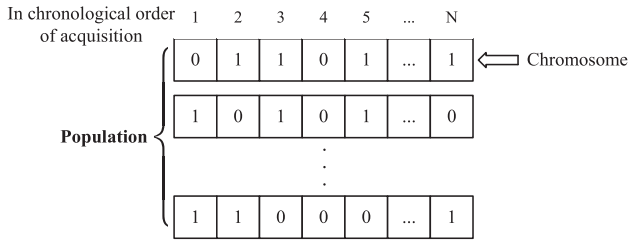

Fig. 8. Binary coding and population. Each chromosome represents a baseline optimization scheme. If the gene on the chromosome is 1, the corresponding acquisition is selected; and if the gene is 0, the corresponding acquisition is not adopted.

A correlation assessment is conducted at intervals of G_g generations, primarily relying on the correlation matrix $\mathbf{\Gamma}$ associated with this chromosome. If in the kth row of the matrix exhibits $\gamma_{\text{unc}}^k > T_c$, it signifies that the contribution of the kth element in Ω from the l_k observation to the overall imaging process is relatively low. Consequently, the value of the l_kth gene on the chromosome is modified from 1 to 0.

3) Preferred Solution: A Pareto solution set is obtained after solving the multiobjective optimization problem using the NSGA-II algorithm, and a simple selection strategy is set to avoid the human subjective factors on the selection of the final result. The spatial-temporal correlation coefficient and the maximum unambiguous height under each solution in the Pareto solution set are calculated to form the objective function matrix $\mathbf{V}^i = [\gamma_{b,t}^i, H_{\max}^i]$. The two objective function values are sorted in order, and the position of the median of each function in the matrix $\mathbf{V}$ is recorded $[p \quad q]$. If $p = q$, the pth solution corresponding to the Pareto solution set is the final selection scheme. If $p \neq q$, the ϕ value of Pareto solution set from the p th solution to the qth solution is calculated according to (32), and the solution corresponding to the smallest ϕ value is taken as the final selection.

$$\phi^i = \omega_1 \frac{\rho_s^i}{\rho_s^{\max}} + \omega_2 \frac{\rho_v^i}{\rho_v^{\max}} \tag{32}$$

where ω_1 and ω_2 are the weights, ρ_s^i and ρ_v^i are the resolution in the elevation direction and deformation direction corresponding to the ith solution in the Pareto solution set, and $\rho_s^{\max}$ and $\rho_v^{\max}$ are the maximum values of the respective resolutions in the solution set.

In the entire algorithm process, spatial baseline, temporal baseline, and correlation coefficient matrix need to be computed repeatedly. To save storage space and computation time, each acquisition data can be used as a reference respectively, and the spatial baseline matrix, temporal baseline matrix, and correlation coefficient matrix are generated after calculating based on their data parameters. The specific procedure is shown in Table II. In the process of baseline optimization, when it is necessary to use the spatial-temporal baseline and correlation coefficient matrix data corresponding to each chromosome's selection scheme, it can be directly selected from the pregenerated matrices according to the serial number, without multiple

TABLE II
PROCEDURE FOR CONSTRUCTING TEMPORAL BASELINE, SPATIAL BASELINE, AND CORRELATION COEFFICIENT MATRICES

Input: All repeat-pass positions $\mathbf{P}$, times $\mathbf{D}$, operating velocities $\mathbf{V}$, the scene's central position P_t, and SNR

Initialize:

$\mathbf{B}$, $\mathbf{T}$, and $\mathbf{\Gamma}$ are zero matrices of size $N \times N$ and $\mathbf{B_c}$ is a zero matrix of size $N \times 1$

for i =1 to N

Select the i th acquisition as the reference.

Compute the spatial baseline B^i, the temporal baseline T^i, the critical baseline B_c^i, and the correlation coefficients Γ^i between the other acquisitions and the reference acquisition.

$$\mathbf{B}(i,:) = B^i,\ \mathbf{T}(i,:) = T^i,\ \mathbf{B_c}(i) = B_c^i,\ \mathbf{\Gamma}(i,:) = \Gamma^i$$

end loop

calculations. Table III describes the key procedural steps for optimizing spatial-temporal baseline.

V. SIMULATION RESULTS AND DISCUSSION

The characteristics of GEO SAR short repeat-pass time enable rapid acquisition of sufficient data. We consider the role of baseline optimization in the short period (1 quarter) and long period (1 year), and evaluated the effectiveness of this method based on the results of 4-D reconstruction.

A. Case I: Short Period of Time

According to the satellite orbit parameters designed in Table I, we simulate the operation of GEO SAR in STK software. To observe the overall trend of baseline changes and reduce data volume, the data are acquired at the frequency of once every two days, and a total of 60 passes of GEO SAR spatial positions in 120 days are obtained. Under the simulation parameters shown in Table IV, we use the proposed baseline optimization method to filter the existing acquisitions and obtain a set of optimal spatial-temporal baseline distributions, as shown in Fig. 9. In the absence of orbit control, the GEO SAR spatial-temporal baseline shows a curved pattern, as discussed earlier. The spatial-temporal baseline obtained by the baseline optimization method is mainly located in the first half of the original distribution. Table V shows the theoretical performance parameters corresponding to different spatial-temporal baseline distributions before and after baseline optimization.

To evaluate the impact of spatial-temporal baselines on the 4-D reconstruction of a scene before and after baseline optimization, a simple scene, as shown in Fig. 10, was constructed for imaging processing. The scene is a common ground plane with a high-rise building structure, and only the radar-facing facade and roof of the building are represented. The scene is placed at the center of the GEO SAR beam pointing on the ground plane, and the SAR image stack is constructed by 2-D imaging of the scene based on the GEO SAR satellite positions.

TABLE III
SPATIAL-TEMPORAL BASELINE OPTIMIZATION PROCESS BASED ON NSGA-II

Initialize the Size of the population N_p, the maximum number of iterations $MaxGen$, crossover probability P_c, mutation probability P_m, and population $Chrom$, where $Chrom$ is a randomly generated Boolean matrix of size $N_p \times N$

Initialize $gen = 0$

while $gen < MaxGen$

(1) Crossover, mutation, and population merging.

(2) Remove duplicate individuals from the population and randomly generate chromosomes to fill population gaps.

(3) Perform Correlation judgment every G_g iterations

for $i = 1$ to N_p

$\mathbf{X} = Chrom(i,:)$

$\Omega = \{\{l_1, l_2, \cdots, l_n\} : x_{l_n} = 1\}$

Extract the combination of rows and columns corresponding to Ω from $\mathbf{\Gamma}$ to form $\mathbf{\Gamma^X}$, $\mathbf{\Gamma^X} = \mathbf{\Gamma}_\Omega$

for $k = 1$ to n

$N_{unc}(k) = \sum_j [P(\mathbf{\Gamma}_{k,j} < \beta)]$

end

compute $\gamma_{unc} = N_{unc} / n$

$\Psi = \{\{r_1, r_2, \cdots, r_u\} : \gamma_{unc}(r_u) > \mathrm{T}_c\}$

$index = \Omega(\Psi)$

$\mathbf{X}(index) = 0$

end if

(4) Calculate the values σ_s, σ_v, $\gamma_{b,t}$, and $H_{\max}$ for each chromosome.

(5) Perform fast non-dominated sorting under multiple constraints for the objective function values $\gamma_{b,t}$ and $H_{\max}$.

(6) Calculate the crowding distance and select N_p individuals for the next generation.

(7) $gen = gen + 1$

end loop

Output:

Obtain a Pareto solution set and get a final solution based on the preferred solution solving strategy

Considering that the GEO SAR elevation resolution is already high enough, we adopt the simpler orthogonal matching pursuit (OMP) algorithm to reconstruct the scene.

Fig. 11(a) and (b) displays the reconstructed scene from corresponding SAR data in the original 60-pass spatial-temporal

TABLE IV
PARAMETER VALUES SET IN THE BASELINE OPTIMIZATION SIMULATION

Parameters	Value
Bandwidth (MHz)	300
Wavelength (m)	0.03
Crossover probability	0.8
Mutation probability	0.04
Elevation estimation threshold T_s (m)	0.5
Deformation velocity estimation threshold T_v (m/day)	1×10^{-4}
Correlation number threshold T_c	0.7

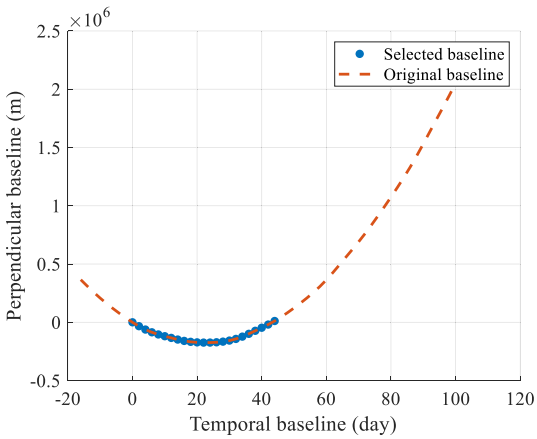

Fig. 9. Spatial-temporal baseline distribution before and after baseline optimization. The red dashed line is the baseline distribution before the baseline optimization, and the blue dots are the baselines after the baseline optimization.

TABLE V
COMPARISON OF GEO D-TOMOSAR PARAMETERS BEFORE AND AFTER BASELINE OPTIMIZATION

Parameters	Before baseline optimization	After baseline optimization
Number of baselines	60	23
Elevation resolution (m)	0.2335	2.9489
Deformation resolution (mm/day)	0.1271	0.3409
Spatial-temporal correlation coefficient	0.8071	0.0462

baseline distribution, while Fig. 11(c) and (d) presents the results of 3-D reconstruction and deformation inversion of the scene from the 23-pass spatial-temporal baseline distribution after baseline optimization. Visually, the corresponding spatial-temporal baseline distribution before and after baseline optimization can both reconstruct the contour shape of the target, and can also intuitively obtain the deformation of the building. However, it is still obvious that the number of spurious points in

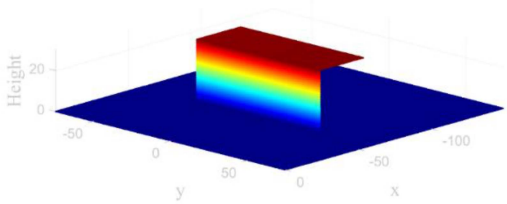

Fig. 10. Imaging scene. The scene simply consists of the ground and a high-rise building façade and roof facing the radar.

the imaging results after baseline optimization is less than that before optimization.

To further quantitatively evaluate the imaging effect before and after baseline optimization, we analyze the ground part with zero elevation and deformation and compare the reconstructed ground point cloud elevation and mean deformation velocity before and after baseline optimization with different forms of spatial-temporal baseline distribution under the same imaging processing. Under the original 60-track spatial-temporal baseline form, the standard deviation of the ground part height estimation is $\sigma_s = 0.1892\,\mathrm{m}$, which is about 2.90 times of the theoretical estimation accuracy, while the standard deviation of the deformation rate estimation is $\sigma_v = 0.1063\,\mathrm{mm/day}$, approximately 26.98 times the theoretical estimation accuracy. After the baseline optimization, the standard deviation of the ground point cloud height estimation is $\sigma_s = 0.2833\mathrm{m}$, approximately 0.90 times the theoretical value, and the standard deviation of the deformation rate estimation is $\sigma_v = 0.0284\mathrm{mm/day}$, approximately 3.13 times the theoretical value. The standard deviation of the parameter estimates is closer to the CRLB after the baseline optimization of the spatial-temporal baseline distribution, which is one of the reasons why the number of spurious points in the differential tomography imaging results after the baseline optimization in Fig. 11 is less than that before the optimization.

B. Case II: Long Period of Time

To verify whether the baseline optimization method can continoue to improve the imaging results during the full working cycle, we obtain the orbital ephemeris of the BeiDou IGSO-5 for one year. At the frequency of sampling once every 3 days, there are 120 acquisitions. The spatial-temporal baseline distribution is shown by the red dotted line in Fig. 12(a), exhibiting an approximate periodic variation. Under the satellite positions of 120 passes, the 2-D SAR imaging of the scene shown in Fig. 10 is performed to obtain the SAR single-look complex image under each repeat pass. The imaging results under the original baseline distribution are shown in Fig. 12(a) and (b). The baseline optimization reduced the number of baselines to 27, as indicated by the blue dots in Fig. 12(a), and the corresponding imaging results are shown in Fig. 12(d) and (e).

Similarly, the estimation results of the elevation and mean deformation velocity of the ground plane are evaluated quantitatively. Under the original baseline, the standard deviation of the estimated ground height was 0.1594 m, which is approximately

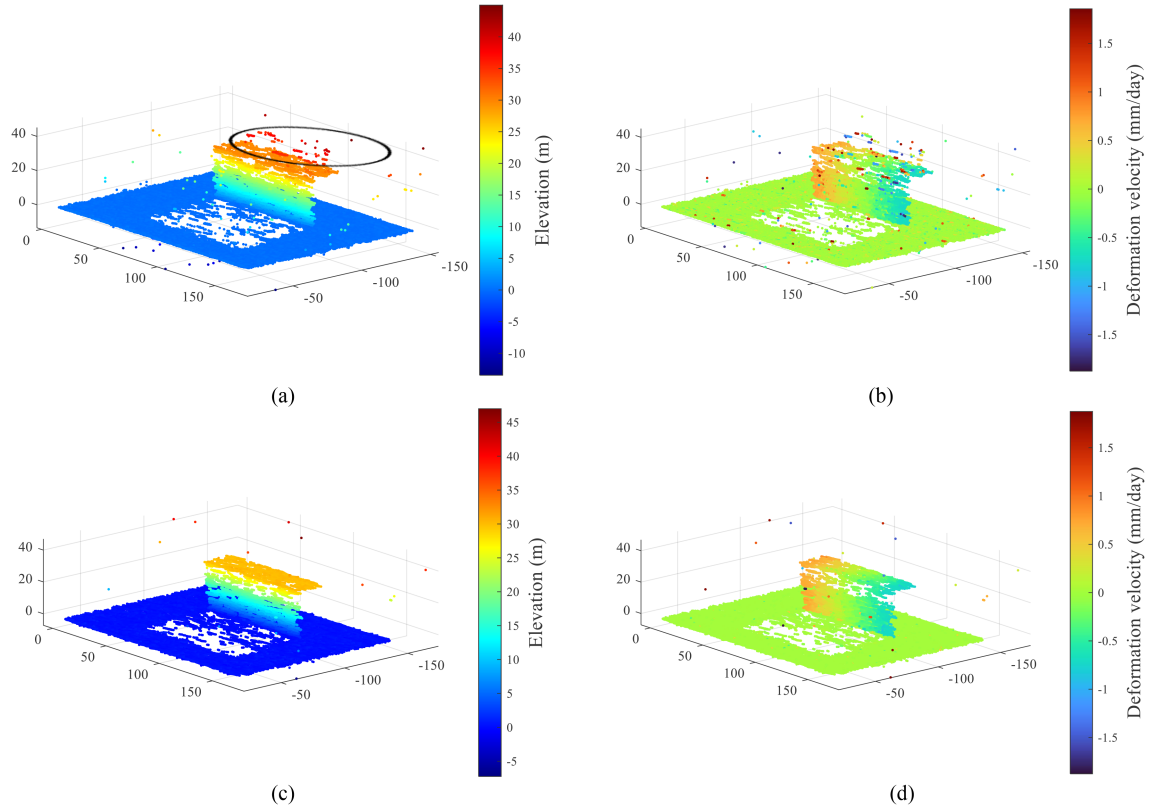

Fig. 11. GEO D-TomoSAR imaging results corresponding to different spatial-temporal baseline distributions. (a) 3-D reconstruction under the original 60-pass baselines. (b) Deformation inversion of the scene under the original spatial-temporal baseline distribution. (c) 3-D reconstruction after baseline optimization. (d) Deformation inversion of the scene under the optimization baseline distribution.

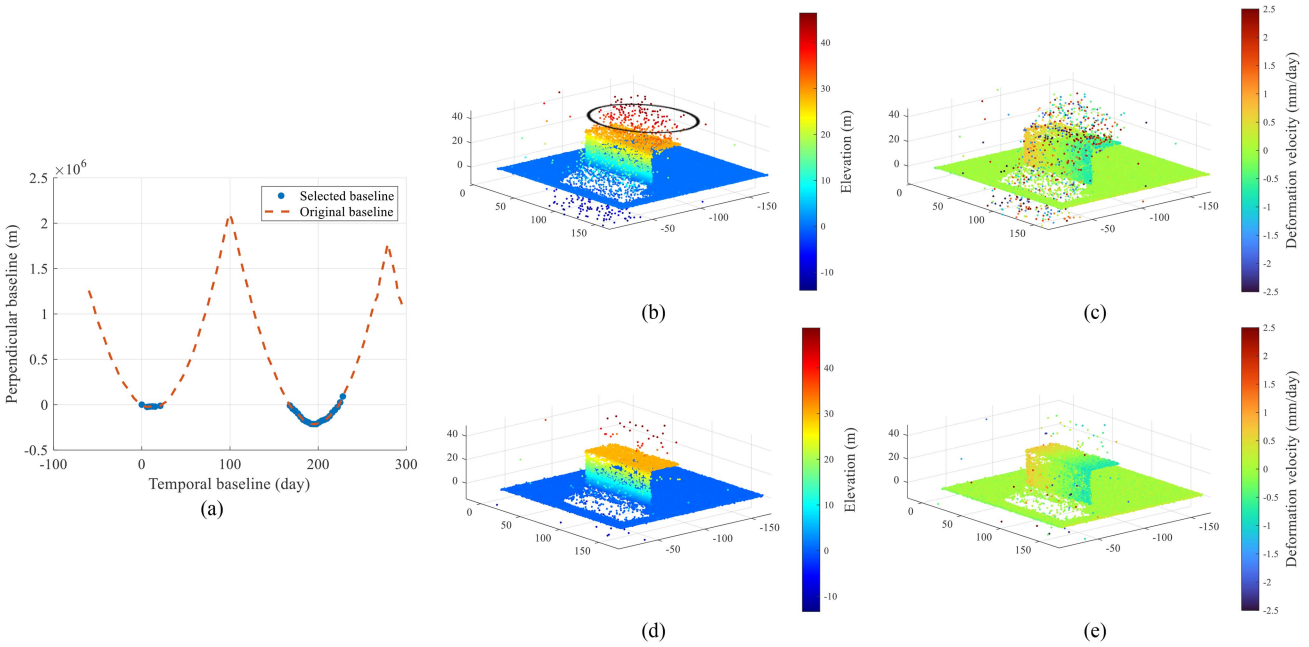

Fig. 12. Baseline distribution and imaging results before and after spatial-temporal baseline optimization for BeiDou IGSO5 within one year. (a) Spatial-temporal baseline distribution. (b) 3-D reconstruction before baseline optimization. (c) Deformation inversion of the scene before baseline optimization. (d) 3-D reconstruction of scene after baseline optimization. (e) Deformation inversion of the scene after baseline optimization.

3.02 times the CRLB. And The standard deviation of mean deformation velocity estimation is $0.0742\,\mathrm{mm/day}$, which is approximately 97.02 times the CRLB. After baseline optimization, the standard deviation of ground plane elevation estimation is $0.2772\mathrm{m}$, about 1.11 times of CRLB, and the standard deviation of mean deformation velocity estimation is $0.1194\,\mathrm{mm/day}$, about 59.19 times of CRLB. In terms of the standard deviation of elevation and mean deformation estimation, the corresponding values under the original baseline are smaller, but the results after baseline optimization are closer to the estimated CRLB.

Through the aforementioned simulation analysis, the unique spatial-temporal baseline distribution of GEO SAR requires spatial-temporal baseline selection before using GEO SAR acquisition data for D-TomoSAR. In addition, increasing the number of baselines is not always beneficial for GEO D-TomoSAR imaging. In fact, adding some baselines can introduce excessive noise and degrade the quality of imaging results. When the original spatial-temporal baseline approximately presents a linear distribution, that is, the spatial-temporal baseline is highly coupled, no matter how optimized the spatial-temporal baseline will not achieve a good effect, which is completely different from TomoSAR. Therefore, the primary focus for further improvement measures will be on enhancing the D-TomoSAR imaging algorithm in the case of high coupling.

VI. Conclusion

In this article, we explore the characteristics of GEO SAR spatial and temporal baselines, which exhibit coupling between the spatial and temporal baselines and show periodic changes in the spatial baselines during the complete operational cycle. The analysis of the CRLB for GEO D-TomoSAR in terms of elevation and mean deformation velocity estimation indicates that the distribution form of the spatial-temporal baseline has a key impact on the imaging performance. Therefore, to reduce the spatial-temporal baseline coupling and improve the D-TomoSAR imaging performance from the dataset construction for the large volume of data, we propose an optimal baseline selection method with the objectives of minimizing the spatial-temporal correlation coefficient and maximizing the maximum unambiguous height to select an optimal set of spatial-temporal baseline from all acquisitions of GEO SAR.

In the simulation, two cases of spatio-temporal baseline distribution of GEO SAR in a short time period and a complete working cycle are considered, respectively. As there is currently no on-orbit GEOSAR system available, it is impossible to obtain real data. To make the experimental results more convincing, we obtained the satellite spatial position based on the ephemeris of BeiDou IGSO-5. We explored the D-TomoSAR imaging results under different spatial-temporal baseline distributions before and after baseline optimization, and quantitatively analyzed the standard deviations of ground plane elevation and mean deformation velocity estimation in simulation scene. The results show that not all acquisitions acquired by the SAR system are suitable for GEO D-TomoSAR imaging, and the baseline optimization can filter out the acquisitions that are not useful for the final results to a certain extent. In the first case, the original 60-pass baseline is optimized to 23 passes. In the second case, the original 120-passes baseline is preferred to 27 passes. After baseline optimization, the elevation estimation approximates to CRLB, and the deformation velocity estimation is closer to CRLB than the original baseline distribution. Visually, baseline optimization reduces the spurious points in the reconstructed point cloud.

Future work will address how the D-TomoSAR imaging algorithm can be improved in the high-coupling case.

References

[1] F. Lombardini, "Differential tomography: A new framework for SAR interferometry," in *Proc. Int. Geosci. Remote Sens. Symp.*, 2003, vol. 2, pp. 1206–1208.

[2] G. Fornaro, D. Reale, and F. Serafino, "Four-dimensional SAR imaging for height estimation and monitoring of single and double scatterers," *IEEE Trans. Geosci. Remote Sens.*, vol. 47, no. 1, pp. 224–237, Jan. 2009.

[3] X. X. Zhu and R. Bamler, "Compressive sensing for high resolution differential SAR tomography—The SL1MMER algorithm," in *Proc. Int. Geosci. Remote Sens. Symp.*, 2010, pp. 17–20.

[4] G. Fornaro, A. Pauciullo, D. Reale, and S. Verde, "Multilook SAR tomography for 3-D reconstruction and monitoring of single structures applied to COSMO-SKYMED data," *IEEE J. Sel. Topics Appl. Earth Observ. Remote Sens.*, vol. 7, no. 7, pp. 2776–2785, Jul. 2014.

[5] X. X. Zhu, Y. Wang, S. Montazeri, and N. Ge, "A review of ten-year advances of multi-baseline SAR interferometry using terraSAR-X data," *Remote Sens.*, vol. 10, no. 9, 2018, Art. no. 1374.

[6] K. Tomiyasu, "Synthetic aperture radar in geosynchronous orbit," in *Proc. Antennas Propag. Soc. Int. Symp.*, 1978, vol. 16, pp. 42–45.

[7] K. Tomiyasu, "Tutorial review of synthetic-aperture radar (SAR) with applications to imaging of the ocean surface," *Proc. IEEE*, vol. 66, no. 5, pp. 563–583, May 1978.

[8] T. Long, C. Hu, Z. Ding, X. Dong, W. Tian, and T. Zeng, *Geosynchronous SAR: System and Signal Processing*. Singapore: Springer, 2018, pp. 1–290.

[9] S. N. Madsen, W. Edelstein, L. D. DiDomenico, and J. LaBrecque, "A geosynchronous synthetic aperture radar; for tectonic mapping, disaster management and measurements of vegetation and soil moisture," in *Proc. Scanning Present Resolving Future. IEEE Int. Geosci. Remote Sens. Symp.*, 2001, vol. 1, pp. 447–449.

[10] S. Hobbs, C. Mitchell, B. Forte, R. Holley, B. Snapir, and P. Whittaker, "System design for geosynchronous synthetic aperture radar missions," *IEEE Trans. Geosci. Remote Sens.*, vol. 52, no. 12, pp. 7750–7763, Dec. 2014.

[11] K. Tomiyasu and J. L. Pacelli, "Synthetic aperture radar imaging from an inclined geosynchronous orbit," *IEEE Trans. Geosci. Remote Sens.*, vol. GE-21, no. 3, pp. 324–329, Jul. 1983.

[12] C. Hu, T. Long, T. Zeng, F. Liu, and Z. Liu, "The accurate focusing and resolution analysis method in geosynchronous SAR," *IEEE Trans. Geosci. Remote Sens.*, vol. 49, no. 10, pp. 3548–3563, Oct. 2011.

[13] G.-C. Sun, M. Xing, Y. Wang, J. Yang, and Z. Bao, "A 2-D space-variant chirp scaling algorithm based on the RCM equalization and subband synthesis to process geosynchronous SAR data," *IEEE Trans. Geosci. Remote Sens.*, vol. 52, no. 8, pp. 4868–4880, Aug. 2014.

[14] B. Hu, Y. Jiang, S. Zhang, Y. Zhang, and T.-S. Yeo, "Generalized omega-K algorithm for geosynchronous SAR image formation," *IEEE Geosci. Remote Sens. Lett.*, vol. 12, no. 11, pp. 2286–2290, Nov. 2015.

[15] C. Hu, Y. Li, X. Dong, R. Wang, and C. Cui, "Optimal 3D deformation measuring in inclined geosynchronous orbit SAR differential interferometry," *Sci. China Inf. Sci.*, vol. 60, pp. 1–15, 2017.

[16] Y. Zhang, W. Xiong, X. Dong, and C. Hu, "A novel azimuth spectrum reconstruction and imaging method for moving targets in geosynchronous spaceborne–airborne bistatic multichannel SAR," *IEEE Trans. Geosci. Remote Sens.*, vol. 58, no. 8, pp. 5976–5991, Aug. 2020.

[17] C. Cui, X. Dong, Y. Li, Z. Chen, and X. Li, "DNN with similarity constraint for GEO SA-BSAR moving target imaging," *IEEE Geosci. Remote Sens. Lett.*, vol. 19, 2022, Art. no. 4512005.

[18] Z. Chen, C. Hu, X. Dong, Y. Li, W. Tian, and S. Hobbs, "Coherence-based geosynchronous SAR tomography employing formation flying: System design and performance analysis," *IEEE Trans. Geosci. Remote Sens.*, vol. 59, no. 9, pp. 7165–7179, Sep. 2021.

[19] C. Hu, Z. Chen, Y. Li, X. Dong, and S. Hobbs, "Research progress on geosynchronous synthetic aperture radar," *Fundam. Res.*, vol. 1, no. 3, pp. 346–363, 2021.
[20] H. Wen, L. Yun, T. Wei-Xian, W. Yan-Ping, and X. Mao-Sheng, "Study on geosynchronous circular SAR," *J. Radars*, vol. 4, no. 3, pp. 241–253, 2015.
[21] C. Hu, B. Zhang, X. Dong, and Y. Li, "Geosynchronous SAR tomography: Theory and first experimental verification using beidou IGSO satellite," *IEEE Trans. Geosci. Remote Sens.*, vol. 57, no. 9, pp. 6591–6607, Sep. 2019.
[22] X. X. Zhu and R. Bamler, "Tomographic SAR inversion by L1-norm regularization-the compressive sensing approach," *IEEE Trans. Geosci. Remote Sens.*, vol. 48, no. 10, pp. 3839–3846, Oct. 2010.
[23] F. Lombardini, "New potentials of differential SAR tomography: Volumetric differential interferometry and robust DEM generation," in *Proc. Int. Geosci. Remote Sens. Symp.*, 2007, pp. 5281–5284.
[24] F. Lombardini and M. Pardini, "Superresolution differential tomography: Experiments on identification of multiple scatterers in spaceborne SAR data," *IEEE Trans. Geosci. Remote Sens.*, vol. 50, no. 4, pp. 1117–1129, Apr. 2012.
[25] X. X. Zhu and R. Bamler, "Let's do the time warp: Multicomponent nonlinear motion estimation in differential SAR tomography," *IEEE Geosci. Remote Sens. Lett.*, vol. 8, no. 4, pp. 735–739, Jul. 2011.
[26] H. Bi, S. Jin, X. Wang, Y. Li, B. Han, and W. Hong, "High-resolution high-dimensional imaging of urban building based on GaoFen-3 SAR data," *J. Radars*, vol. 11, no. 1, pp. 40–51, 2022.
[27] X. Sun, "Study on SAR tomography and differential tomography imaging," Ph.D. dissertation, Dept. Elect. Eng., Nat. Univ. Defense Technol., Changsha, China, 2012.
[28] D. Reale, G. Fornaro, and A. Pauciullo, "Extension of 4-D SAR imaging to the monitoring of thermally dilating scatterers," *IEEE Trans. Geosci. Remote Sens.*, vol. 51, no. 12, pp. 5296–5306, Dec. 2013.
[29] A. Budillon, A. C. Johnsy, and G. Schirinzi, "Extension of a fast GLRT algorithm to 5D SAR tomography of urban areas," *Remote Sens.*, vol. 9, no. 8, 2017, Art. no. 844.
[30] C. Hu, B. Zhang, X. Dong, Y. Li, and C. Cui, "Optimal data acquisition in multi-pass geosynchronous SAR tomography," *J. Eng.*, vol. 2019, no. 20, pp. 6359–6363, 2019, doi: 10.1049/joe.2019.0383.
[31] W. Zhidong, T. Xinming, and L. Tao, "Impact analysis of InSAR spatio-temporal baseline on DEM accuracy," *Bull. Surveying Mapping*, vol. 64, no. 2, pp. 61–66, 2018.
[32] D. T. S. Kelso, *NORAD GP Data Sets Historical Archives*, 2021-2022. [Online]. Available: http://celestrak.org/NORAD/archives/request.php?FORMAT=tle
[33] X. X. Zhu and R. Bamler, "Super-resolution power and robustness of compressive sensing for spectral estimation with application to spaceborne tomographic SAR," *IEEE Trans. Geosci. Remote Sens.*, vol. 50, no. 1, pp. 247–258, Jan. 2012.
[34] H.-P. Xu, Y.-Q. Zhou, and C.-S. Li, "The optimal across-track baseline of distributed small satellites synthetic aperture radar for terrain elevation measurement," *J. Electron. Inf. Technol.*, vol. 28, no. 2, pp. 340–344, 2006.
[35] K. Deb, A. Pratap, S. Agarwal, and T. Meyarivan, "A fast and elitist multiobjective genetic algorithm: NSGA-II," *IEEE Trans. Evol. Comput.*, vol. 6, no. 2, pp. 182–197, Apr. 2002.

Xichao Dong (Member, IEEE) received the B.S. degree in electrical engineering and the Ph.D. degree in target detection and recognition from the Beijing Institute of Technology (BIT), Beijing, China, in 2008 and 2014, respectively.

From 2011 to 2013, he was a Research Assistant with Centre for Terrestrial Carbon Dynamics (CTCD), University of Sheffield, Sheffield, U.K. From 2014 to 2017, he was in a postdoctoral position with the School of Information and Electronics, BIT. Since 2017, he has been with the School of Information and Electronics, BIT, where he was promoted to be an Associate Professor in 2021. His research interests include geosynchronous synthetic aperture radar and weather radar.

Dr. Dong was a recipient of IEEE CIE International Radar Conference Excellent Paper Award in 2011 and the Chinese Institute of Electronics Youth Conference Poster Award in 2014.

Yan Liu received the B.S. degree in electronic information engineering from Xidian University, Xi'an, China, in 2021. She is currently working toward the M.S. degree in information and communication engineering with the Beijing Institute of Technology (BIT), Beijing, China.

Her research interests include geosynchronous synthetic aperture radar differential tomography.

Zhiyang Chen was born in Fujian, China, in 1993. He received the B.S. degree in electronic information science and technology from the Department of Electronic Engineering, Tsinghua University, Beijing, China, in 2016, and the Ph.D. degree in information and communication engineering from the School of Information and Electronics (SIE), Beijing Institute of Technology (BIT), in 2021.

He is currently a Postdoctoral Researcher with the SIE, BIT. His research interests include geosynchronous synthetic aperture radar (SAR) satellites formation design, SAR interferometry, and SAR tomography

Xinyan Chen was born in Shandong, China, in 1998. She received the B.S. degree of intelligence science and technology in School of Information Science and Technology from Sun Yat-sen University (SYSU), Guangdong, China, in 2019. She is currently working toward the Ph.D. degree in information and communication engineering with the Beijing Institute of Technology (BIT), Beijing, China.

Her research interests include synthetic aperture radar (SAR) system and signal processing, tomography SAR interferometry (TomoSAR) technique, and superresolution imaging technology in GEO SAR.

Yuanhao Li (Member, IEEE) received the B.S. degree in information engineering and the Ph.D. degree in information and communication engineering from the Beijing Institute of Technology (BIT), Beijing, China, in 2012 and 2018, respectively.

From 2016 to 2017, he worked as a Visiting Researcher with the Dipartimento di Elettronica e Informazione, Politecnico di Milano, Milan, Italy. In 2018, he was a Research Scientist with the Radar Research Lab, BIT. Between 2018 to 2021, he was a Postdoctoral Researcher with the Department of Geoscience and Remote Sensing, Delft University of Technology, Delft, The Netherlands. He is currently an Associate Professor with the School of Information and Electronics, BIT. His research interests include radar system design and signal processing, InSAR/D-InSAR technique, and radar altimeters constellations.

Dr. Li was the recipient of the Chinese Institute of Electronics Youth Conference Excellent Paper Award in 2014.

Cheng Hu (Senior Member, IEEE) received the B.S. degree in electronic engineering from the National University of Defense Technology, Changsha, China, in 2003, and the Ph.D. degree in target detection and recognition from the Beijing Institute of Technology (BIT), Beijing, China, in 2009.

He was a Visiting Research Associate with the University of Birmingham, Birmingham, U.K., for 15 months, from 2006 to 2007. Since 2009, he has been with the School of Information and Electronics, BIT, and promoted to be a Full Professor in 2014, a Doctoral Supervisor, and the Vice-Director of the Radar Research Lab. He has authored more than 60 SCI-indexed journal articles and more than 100 conference articles. His main research interests include new concept synthetic aperture radar imaging and the biological detection radar system and signal processing.

Feifeng Liu (Member, IEEE) received the B.S. degree in mathematics and the Ph.D. degree in target detection and recognition from the Beijing Institute of Technology (BIT), Beijing, China, in 2002 and 2013, respectively.

He joined the Microwave Integrated System Laboratory, University of Birmingham, Birmingham, U. K., as a visiting student in 2010. Since 2013, he has been a faculty member with the BIT. His research interests include imaging technology of bistatic synthetic aperture radar (SAR) and geosynchronous SAR as well as change-detection technology based on space–surface bistatic SAR systems.